Statistical geometry of particle packings.   II. ''Weak spots'' in liquids

Srikanth Sastry,[1,*] Pablo G. Debenedetti,[1] and Frank H. Stillinger[2,3]

[1]*Department of Chemical Engineering, Princeton University, Princeton, New Jersey 08544*
[2]*Bell Laboratories, Lucent Technologies, Murray Hill, New Jersey 07974*
[3]*Princeton Materials Institute, Princeton University, Princeton, New Jersey 08544*

We investigate the statistical geometry of inherent structures (mechanically stable arrangements of particles generated by a steepest-descent mapping of equilibrium configurations to local potential minima) of liquid configurations of the shifted-force Lennard-Jones system, as an approach to elucidating mechanisms for the decay of metastable states. For a wide range of densities, including some higher than the triple point density, inherent structures are found to display remarkably heterogeneous geometry, with an apparently bicontinuous structure consisting of a compact phase and a void region. The void region is found to consist of a single system-spanning cavity. The volume fraction of this cavity vanishes above the density $\rho^* = 0.89$. This density coincides with the minimum in the pressure vs density curve for inherent structures, at negative pressure, indicating that the observed heterogeneity of the inherent structures is triggered by the crossing of a threshold of mechanical instability, much like the familiar spinodal concept. Analysis of spontaneous density fluctuations in the equilibrium and superheated liquid reveals that atoms present in regions of low density (weak spots) map predominantly to the cavity interface in the inherent structures. We discuss the relevance of these observations to limits of stability of the metastable liquid, nucleation, and, possibly, the glass transition. [S1063-651X(97)09811-5]

PACS number(s): 61.20.Gy, 64.60.My, 64.60.Qb, 64.70.Fx

I. INTRODUCTION

On account of their great structural diversity at the molecular level, substances in the liquid state present a marked contrast to their counterparts in the crystalline state. This diversity eliminates long-range periodic order, while supporting substantial short-range order that can be partially revealed by x-ray and neutron diffraction experiments [1]. It also lies at the heart of hydrodynamic flow and diffusion properties in liquids, attributes that are absent or at least strongly suppressed in the crystalline state. Liquid-state theory has attained substantial quantitative progress in characterizing that structural diversity and its implications for both static and dynamic properties [1,2]. Nevertheless, full understanding remains beyond reach at present. The project reported below was designed to move closer to that goal.

We have focused our efforts on determining and interpreting various aspects of the statistical geometry of fluctuating void space in the liquid state. This collection of properties irreducibly involves high order particle correlations, and thus requires powerful algorithmic tools for study as explained below. We find that the computational study of void space in liquids provides fresh insight into, and suggests new and interesting questions about, the rigorous statistical mechanics of metastability [3], nucleation in superheated liquids, loss of mechanical strength in liquids and glasses, the glass transition, and the ''energy landscape'' (potential energy hypersurface) of liquids.

A simple, classical many-body system serves as the primary source for our results. However, we believe its implications have far wider application, at least qualitatively.

Equilibrium liquid states have been included in our study, but metastable superheated and stretched liquid states also receive considerable attention. Sufficiently large voids that have spontaneously formed in the latter metastable circumstances constitute ''weak spots'' that preferentially serve as nucleation sites for boiling or cavitation [4].

Historical balance requires mentioning that several attempts to develop ''hole'' theories of the liquid state appeared a few decades ago [5–7]. These analyses were also concerned with voids in the medium and their role in determining thermodynamic and transport properties. Judged by present day standards, the authors of these prior works were severely handicapped by lack of information about realistic molecular interactions and the geometric packing arrangements they produce. Subsequent dramatic advances in computational quantum mechanics and in statistical mechanical simulation techniques now enable development of far more powerful ''hole'' or ''void'' descriptions of local order in liquids [3].

Section II below describes the specific model used in our calculations, and states some of its elementary properties. Section II also provides details of the Monte Carlo simulation routine, and of the related procedure that generates inherent structures (local potential energy minima). Section III presents our results for the void distributions from a wide range of equilibrium and metastable liquid states, as well as the corresponding void distributions for their inherent structures. The mapping from liquid configurations to inherent structures generates a remarkable particle segregation, and allows separation of particles into ''surface'' and ''bulk'' categories; Sec. IV documents this feature quantitatively, and suggests a possible connection with the glass transition. The statistical geometry of fluctuating void space presented in Secs. III and IV has interesting implications for the process

*Electronic address: sastry@kanga.princeton.edu

of homogeneous nucleation in stretched and superheated liquids, and for the superheated liquid spinodal at low temperatures. These are discussed in Sec. V. Finally, Sec. VI summarizes the most significant findings, and suggests further implications and directions for future investigation.

II. MODEL SYSTEM

A finite cutoff version of the Lennard-Jones 12-6 potential forms the basis for our numerical simulations. The total interaction potential in an N-particle system for this model has the form

$$\Phi(\mathbf{r}_1,\mathbf{r}_2,\ldots,\mathbf{r}_N)=\epsilon\sum_{i<j} v_c(r_{ij}/\sigma), \qquad (1)$$

where

$$v_c(x)=\begin{cases} 4(x^{-12}-x^{-6})+c_0+c_1(2.5-x), & x<2.5 \\ 0, & x\geq 2.5 \end{cases} \qquad (2)$$

with

$$c_0=0.016\,316\,891, \quad c_1=0.038\,999\,477. \qquad (3)$$

Note that both v_c and its first derivative v_c' are continuous at the cutoff value 2.5.

The full Lennard-Jones pair interaction

$$v_{LJ}(x)=4(x^{-12}-x^{-6}) \qquad (4)$$

vanishes at $x=1$, and passes through a unit depth minimum at $x=2^{1/6}=1.122\,462\ldots$. By contrast v_c vanishes at

$$x_0=1.003\,208 \qquad (5)$$

and its minimum is displaced slightly outward and upward:

$$v_c(x_{\min})=-0.929\,973\ldots, \quad x_{\min}=1.123\,149. \qquad (6)$$

When N is large, Φ in Eq. (1) attains its absolute minimum at vanishing external pressure when the particles are arranged in a hexagonal close packed (hcp) crystal, with nearest neighbor distance $a^*\equiv a/\sigma$, number density $\rho^*\equiv\rho\sigma^3$, and potential energy per particle $\phi^*\equiv\Phi/N\epsilon$ exhibiting the following values:

$$a^*=1.101\,526, $$

$$\rho^*=1.058\,110, $$

$$\phi^*=-6.658\,894. \qquad (7)$$

This model attains almost the same stability in the face-centered cubic (fcc) crystal at zero pressure, but with slightly shifted values:

$$a^*=1.101\,672, $$

$$\rho^*=1.057\,689, $$

$$\phi^*=-6.654\,082. \qquad (8)$$

It should be noted in passing that the unmodified Lennard-Jones case, Eq. (4), also favors the hcp crystal over the fcc

crystal, in the large system limit at zero pressure [8]. The triple point temperature, pressure, and liquid density have been estimated for our v_c model [3]:

$$k_B T_t/\epsilon=0.687, $$

$$P_t\sigma^3/\epsilon=0.003\,061\,9, $$

$$\rho_{lt}\sigma^3=0.67. \qquad (9)$$

The corresponding estimates for the location of the liquid-vapor critical point are [3]

$$k_B T_c/\epsilon=1.16, $$

$$P_c\sigma^3/\epsilon=0.109, $$

$$\rho_c\sigma^3=0.247. \qquad (10)$$

Results from two sets of simulations are presented in this paper. In both cases, the simulations were performed for 256 particles in the (N,V,T) ensemble for the shifted-force Lennard-Jones potential above [Eqs. (1)–(3)]. We also simulated a system of 1372 particles at one particular state point $\rho^*=\rho\sigma^3=0.725$, $T^*=k_B T/\epsilon=0.9$.

The first set of simulations were performed using the canonical Monte Carlo algorithm, at a reduced temperature value of $T^*=k_B T/\epsilon=2.5$ which is substantially higher than the liquid-gas critical temperature. Simulations were performed for a series of reduced density values ranging from $\rho^*=0.6$ to 1.05. In each case, the system was equilibrated for 1000 Monte Carlo cycles, and equilibrated configurations were generated for 3000 Monte Carlo cycles. Configurations every 100 Monte Carlo cycles apart were then used to generate 30 inherent structures, using the procedure described below. For both the equilibrated fluid configurations and the corresponding inherent structures, the void space was analyzed as described below.

The second set of simulations were performed using the inherent structure void-constrained ensemble described in Ref. [3], at a fixed reduced density $\rho^*=0.7$, for temperatures ranging from very high ($T^*=15.0$) to low values ($T^*=0.56$) where the system is metastable with respect to formation of the vapor phase. In the inherent structure void-constrained ensemble, the inherent structures generated periodically (every 100 Monte Carlo cycles) are constrained not to contain voids exceeding a predefined cutoff size. Whenever an inherent structure at the end of a block of 100 Monte Carlo cycles is found to possess voids exceeding the cutoff size, the preceding block of configurations is disregarded and the simulation is started afresh from the configuration at the end of the preceding block. The cutoff parameter $b=d_{\max}\rho^{1/3}$ (where $d_{\max}$ is the maximum allowed void diameter) is set to be $b=6$ in this group of simulations. Thus no void can form in the inherent structure with diameter greater than six times the average interparticle separation. As shown in [3], the constraint resulting from this value of the cutoff is not severe, as reflected in its influence on the measured thermodynamic properties. The role of the constraint is to prevent the metastable system from phase separating. In these runs, the system is equilibrated for 4000 Monte Carlo cycles, and equilibrated configurations are generated for 10 000

cycles. Inherent structures are produced every 100 cycles. Thus the final output contains a sample of 100 inherent structures. As discussed in [3,4], the rigorous statistical mechanics of metastability is the statistical mechanics of systems under constraints. Both the present work and that of [3] are examples of the computational implementation of constraints to study superheated liquids rigorously.

Inherent structures are local potential energy minima to which chosen instantaneous configurations map under a steepest-descent minimization of the energy. In the present case, the appropriate mapping is generated by the following steepest-descent equations for each particle i [9]:

$$\frac{d\mathbf{r}_i(s)}{ds} = -\mathbf{\nabla}_i\Phi[\mathbf{r}_1(s),\ldots,\mathbf{r}_N(s)], \qquad (11)$$

where $s \geq 0$ is a progress variable indicating the extent to which the descent trajectory has been followed. Starting from an initial configuration ($s=0$), a positive value of s displaces the configuration along the direction of the negative of the potential energy gradient until it comes to rest ($s \to \infty$) at the appropriate minimum. Given an initial configuration of N particles, the simultaneous solution of the N equations in Eq. (11) quenches the system into a potential energy minimum, yielding the appropriate inherent structure.

Potential energy minimizations for the shifted-force Lennard-Jones fluid (described above) were performed using the conjugate gradient method [10]. Details of the procedure may be found in Ref. [3].

III. VOID DISTRIBUTIONS

The analysis of void space in simulated equilibrium configurations and inherent structures begins with the construction of the Voronoi and Delaunay tessellation of the configurations [11]. The Voronoi and Delaunay tessellation, illustrated in Fig. 1, is defined as follows: a point $\mathbf{x}$ (where $\mathbf{x}$ is a vector denoting location in space with respect to some origin) belongs to the Voronoi cell of atom i located at position $\mathbf{x}_i$ if it is closer to $\mathbf{x}_i$ than to any other point $\mathbf{x}_j$ of the system. Mathematically, this can be represented by

$$\mathbf{x} \in V_i \Leftrightarrow |\mathbf{x}-\mathbf{x}_i| < |\mathbf{x}-\mathbf{x}_j| \quad \forall j, \qquad (12)$$

where V_i denotes the Voronoi polyhedron which surrounds atom i. The dual Delaunay construction is a tiling of space by simplices (d-dimensional "tetrahedra" where d is the system's dimension) whose vertices are the atom positions $\mathbf{x}_i$, while the centers of the spheres circumscribing these simplices are the Voronoi vertices. For the purpose of characterizing void space, we find it convenient to introduce the following definitions.

(1) The radius of the circumscribing sphere centered on a Voronoi vertex is called the "vertex radius."

(2) The diameter of the circumsphere minus the Lennard-Jones diameter σ is termed the "void size" and is taken as the effective size of the void region about a Voronoi vertex. This amounts to visualizing the voids as spherical particles with diameters equal to their effective size.

(3) For the purpose of analyzing the connectivity of void space, an "exclusion radius" is assigned to each atom, equal to the Lennard-Jones diameter σ. With this choice, a *cavity*
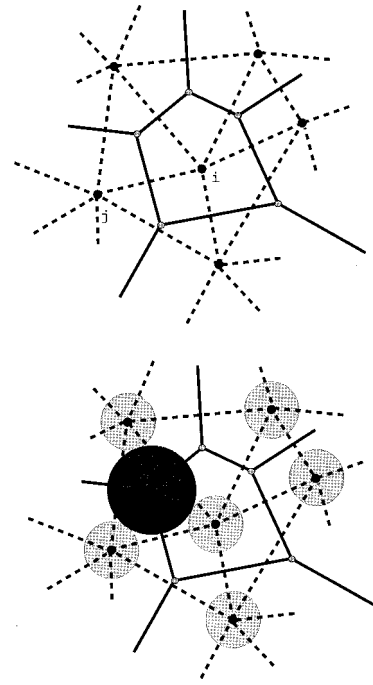

FIG. 1. (top) Two-dimensional illustration of the Voronoi-Delaunay dual construction. Atoms are shown as dark small dots. The central atom i is surrounded by atoms j. The solid lines form the Voronoi polygon about atom i. The dashed lines form the Delaunay triangles whose circumspheres are centered at the corresponding vertices of the Voronoi polygon. (bottom) The determination of the size (diameter) of "void particles." The atoms, shown as lightly shaded circles, lie on the vertices of the Delaunay triangles. The void particles are centered on the vertices of the Voronoi polygon. For clarity, only one void particle is shown (larger, darkly shaded circle). Its diameter (size) equals that of the circle circumscribing the Delaunay triangle and centered on the vertex of the Voronoi polygon, minus the diameter of the atoms.

[12] is any set of mutually connected points in space where an additional atom can be inserted such that its Lennard-Jones sphere (with diameter σ) does not overlap that of any other atom. Equivalently, only those Voronoi vertices with void size $\geq \sigma$ are considered to be in the void.

As observed in Ref. [3], the void size distribution obtained for inherent structures differs remarkably from that for the corresponding equilibrium configurations, displaying a long tail extending up to $\sim 4\sigma$. Correspondingly, a visual inspection of these inherent structure configurations indicates that the particles in the system are arranged in a dense packing, leaving an apparently connected part of the system volume empty [3]. Further, a double peak is found at small void sizes, which is associated with the presence of distorted tetrahedral and octahedral voids in the dense packed region. Similar results for small void sizes were also obtained by Finney and Wallace [13], who generated dense amorphous packings by allowing packings of hard spheres to relax under a smooth repulsive potential.

Figure 2 shows an inherent structure configuration for a system of 1372 particles, generated from a conjugate gradient minimization of the energy of a liquid configuration at $\rho^*=0.725$ and $T^*=0.9$. The particles shaded light gray form the interface between the region where atoms are packed densely, and an empty region. The atoms in the dense
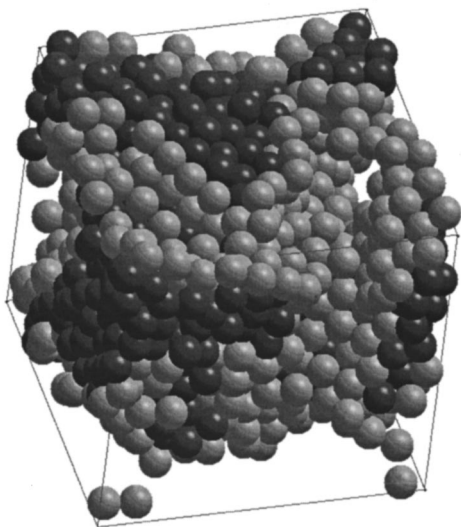
FIG. 2. Configuration of $N=1372$ atoms in an inherent structure obtained from an equilibrated liquid configuration at $T^*=0.9$ and $\rho^*=0.725$. The atoms shaded light gray form the interface of the single cavity present. Atoms in the bulk part (not adjacent to the cavity) are shaded dark gray. If a Voronoi vertex is (not) part of the largest cavity, atoms at the vertices of the dual Delaunay simplex are classified as surface (bulk) atoms.

region are shaded dark gray. It can be seen that the morphology of the packing of atoms is intricate. The empty space occupies a significant fraction of the total volume, and appears to be interconnected.

Figure 3 shows a comparison of void size distributions for equilibrated liquid configurations and corresponding inherent structures at $\rho^*=0.7$. The temperature of the equilibrated liquid is $T^*=0.6$. In an effort to make these observations more precise, and to study the change in the observed features with the system density, we first consider the void size
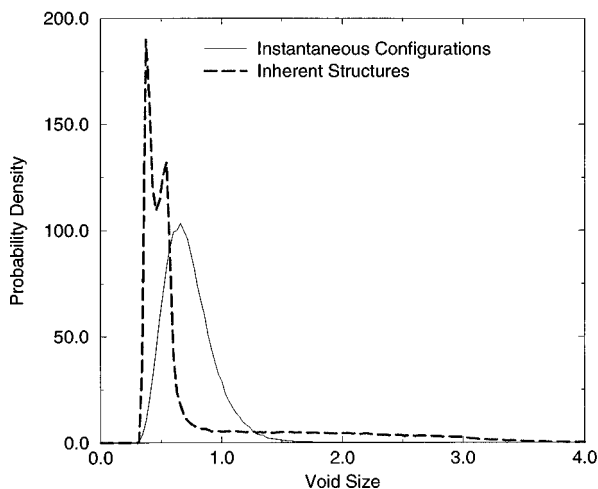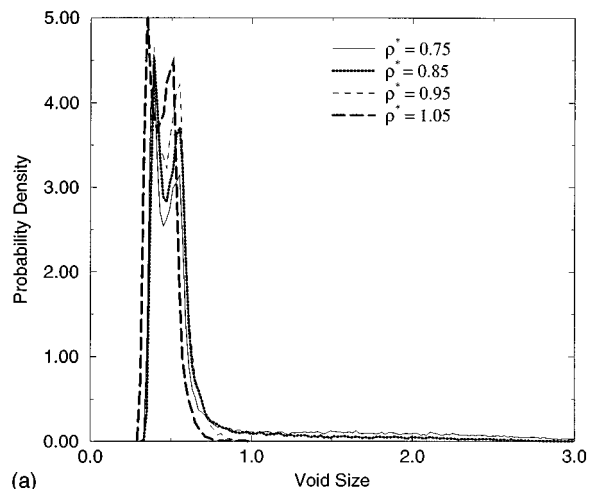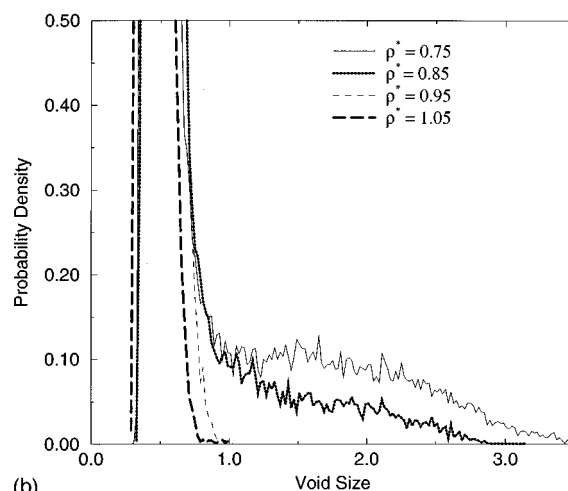

FIG. 3. Probability density of the diameter (in units of σ) of voids found in the inherent structure and in the unquenched liquid for the shifted-force Lennard-Jones fluid at $T^*=0.6$ and $\rho^*=0.7$. The dashed line corresponds to the inherent structures and the solid line corresponds to the unquenched configurations.

FIG. 4. (a) Probability density of the diameter of voids (in units of σ) found in the inherent structures of the shifted-force Lennard-Jones fluid as a function of density. Note that while for $\rho^*=0.75$, 0.85 the peak positions roughly coincide, they move to lower values for $\rho^*=1.05$. (b) Detail of the void size distribution as shown in (a), but here on a different x,y-axis scale. Note that the "tail" of the void size distribution disappears at higher densities.

distributions, and then analyze the connectivity properties of the void space.

Figure 4(a) shows the void size distributions for four densities ($\rho^*=0.75,0.85,0.95,1.05$). In all cases, the temperature of the equilibrated configurations from which the inherent structures were obtained was $T^*=2.5$. Two trends in these distributions are visible. As the density increases, the low void size peaks ("double peak") do not at first change location appreciably. In Fig. 4, $\rho^*=0.75,0.85$ represent the range of densities where this behavior is observed. However, at high densities, the peak positions move to lower values, as seen for $\rho^*=1.05$. The second trend in behavior is observed in the tail of the distribution. While the two lower densities exhibit a large void tail (the range being smaller for $\rho^*=0.85$ compared to $\rho^*=0.75$), no tail is observed for the two higher densities. Figure 4(b) shows the same distributions on a magnified y-axis scale to make this point clearer.

We consider next the connectivity and extent of the void space associated with these void distributions. The void size
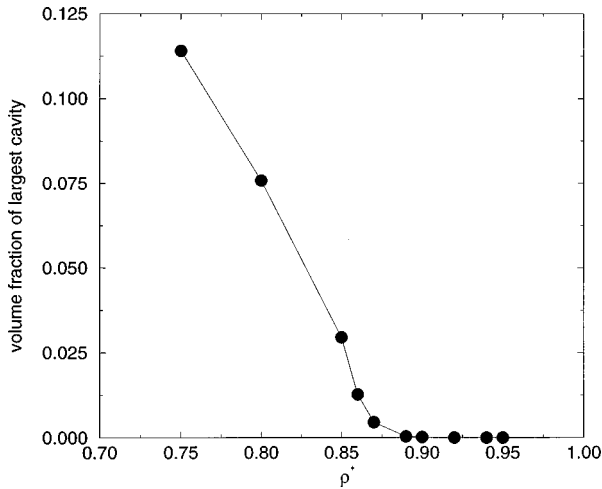
FIG. 5. Volume fraction of the largest cavity in inherent structures as a function of density. Note that this volume fraction vanishes at $\rho^* = 0.89$.

FIG. 6. Separation of void size distribution into bulk and cavity components for $T^* = 1.5$, $\rho^* = 0.7$. Note that the separation is sharp at the exclusion radius defining the void ($r_c = \sigma$, which is equivalent to void size equal to 1 (in units of σ).

distribution, while characterizing the empty space in a fashion useful for constrained ensemble simulations, does not provide a complete description of void space. For example, the fraction of the system's volume that is empty of particles (void space volume fraction) cannot be obtained directly from the void size distribution. In addition, it is important to understand how the void space is connected; i.e., whether the void space present in the system can be decomposed into many disconnected cavities, or whether all the void space present in the system is connected and mutually accessible. To obtain this information, we have developed an algorithm that can (a) identify disconnected cavities that exist in the system, and (b) yield the total void volume present in each cavity. The details of this algorithm are presented in part I of this work [12]. We note here that part of the procedure distinguishes Voronoi vertices that contribute to the total void from those that do not. In order to generate the above information, we must define an exclusion radius around each atom, which separates space into occupied and unoccupied (or void) volume. We choose the exclusion radius to be $r_c = \sigma$, the Lennard-Jones diameter. Hence voids whose diameter is smaller than σ do not contribute to the total void space, because it is impossible to insert another Lennard-Jones atom in such voids without overlap of its Lennard-Jones sphere with those of the other atoms in the surrounding Delaunay tetrahedron.

Figure 5 shows the volume fraction of the largest cavity as a function of density. We see that at a density $\rho^* \sim 0.89$, the void volume fraction essentially vanishes. At higher densities, no void volume is present. We find that in a majority of the configurations analyzed, the bulk of the void volume is contained in a single cavity. The average number of cavities varies from ~ 1 at low densities ($\rho^* = 0.6, 0.7$) to a maximum of 2.45 at $\rho^* = 0.87$, close to the density $\rho^* \sim 0.89$ where the void volume fraction becomes insignificant. In the range of densities where the average number of cavities deviates significantly from 1 ($\rho^* = 0.85 - 0.89$), the void volume fraction contained in cavities other than the largest cavity does not exceed 5%. We conclude that the void volume consists predominantly of a single connected cavity. Given the modest system sizes studied here, the asymptotic morphology of in-
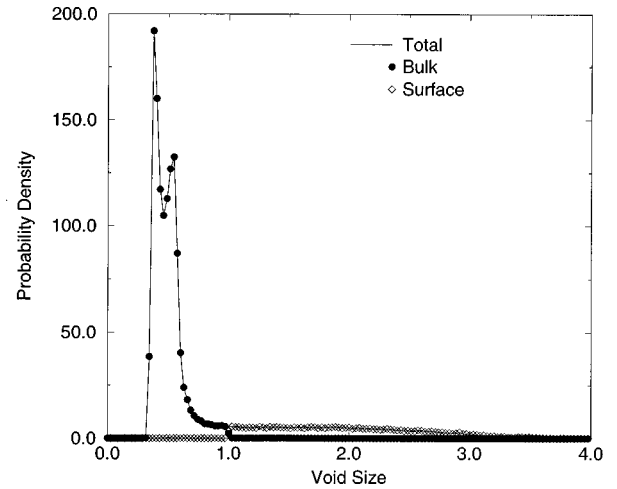
herent structures as the system size increases remains to be studied. We summarize our expectation of the morphology of inherent structures for large systems, and the reasoning behind our expectation, in Appendix B.

IV. SURFACE AND BULK PARTICLES

The identification of the cavity containing the void volume permits us to separate the void size distribution into bulk and cavity components, wherein the bulk component is formed by comparing the probability density of distances of the Voronoi vertices from atom centers for vertices that do not lie in the cavity, while the cavity component is formed by considering Voronoi vertices that lie in the void. Figure 6 shows these two component distributions. It is observed that there is a sharp change when the vertex radius equals the exclusion radius.

The separation of Voronoi vertices into bulk and cavity vertices also permits us to distinguish two types of atoms. Atoms that lie at the vertices of the Delaunay simplex dual to a Voronoi vertex which is in the void predominantly constitute the surface of the largest cavity. If the Voronoi vertex is not part of the largest cavity, the atoms at the vertices of the dual Delaunay simplex are classified as belonging to the bulk. We label atoms as either surface atoms or bulk atoms, according to this criterion. As first shown in [3], visual inspection of the inherent structures obtained from liquid states near the triple point density reveals a dense amorphous phase (bulk), and a large, possibly system-spanning void. The atoms that we label as surface atoms form the interface between the amorphous bulk phase and the void space. The bulk or surface classification permits us to calculate the average density in the bulk component of the inherent structures. This is done by calculating the ratio of the number of bulk atoms to the sum of volumes of their Voronoi cells, since each Voronoi cell by definition contains one atom. Figure 7 shows the variation of the density of the bulk and surface parts of the inherent structures as a function of the system density. We notice the remarkable fact that the density of the bulk component of the system increases as the
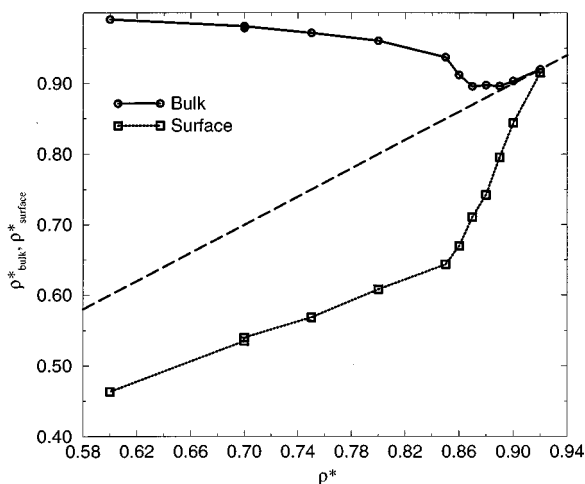
FIG. 7. Variation of density of the bulk and cavity components of inherent structures with the total density of the system. The straight (dotted) line with unit slope ($x=y$) is also shown as reference.

total density decreases. The density of the bulk component becomes equal to the overall density at $\rho^* \sim 0.89$. The density associated with surface particles does not, since cavities with finite (if extremely small) volume persist until $\rho^* = 0.92$, and as a result yield lower values for the densities of surface atoms. However, the number of such atoms is extremely small for $\rho^* = 0.90$ and 0.92.

In seeking an explanation of this behavior, we calculate the pressure experienced by the inherent structures. Theoretical and methodological details germane to this calculation are discussed in Appendix A. Over the range of densities investigated, the equation of state (pressure vs density) of the inherent structures displays van der Waals–type behavior, as shown in Fig. 8. Starting at high density, decreasing the density gradually places the inherent structures under tension. At $\rho^* = 0.89$, the limit of maximum tension is reached. Upon further expansion, the pressure increases instead of decreasing. This is exactly the density at which voids appear in the inherent structure, whose inhomogeneity at $\rho^* < 0.89$ is
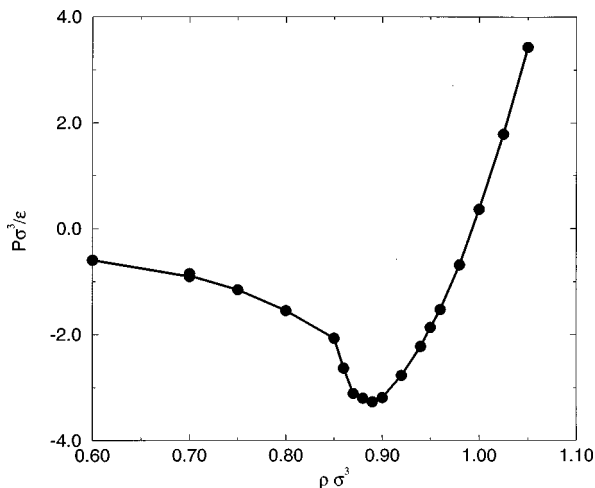

FIG. 8. Variation of the pressure of inherent structures with the system density. Note that the minimum in this curve coincides with the density at which the void volume vanishes.

therefore the result of a mechanical instability. Thus the appearance of void space in the inherent structures and the progressive densification of the bulk component below $\rho^* = 0.89$ appear to be consequences of the system reaching a density of mechanical instability, below which the system becomes heterogeneous, simultaneously lessening the tensile stress it bears. Since a glass is simply a liquid trapped in an inherent structure [14], Figs. 7 and 8 suggest the interesting question of whether this mechanical instability can be considered the absolute lower limit below which a glass cannot exist. We are studying this question. The equation of state of inherent structures (pressure vs density) was previously considered by LaViolette [15]. However, its relationship to changes in the void geometry discussed here has not been previously reported.

At $\rho^* \sim 0.993$, the inherent structures experience zero pressure. Amorphous packings prepared under conditions free of external pressure (e.g., vapor deposition) would possess this density. Of course, the precise value of the packing density is a function of the intermolecular potential.

V. IMPLICATIONS FOR NUCLEATION, AND THE SPINODAL CURVE

The above results show that the mechanically stable configurations of a simple atomic liquid become inhomogeneous below a certain bulk density due to the appearance of large voids. We now investigate some implications of this interesting observation for homogeneous nucleation in superheated liquids.

Superheated liquids will transform irreversibly into the vapor phase. In the absence of dissolved or suspended impurities or foreign surfaces, this transformation necessitates the formation of large enough bubbles within the bulk liquid. This is an example of homogeneous nucleation, in which the stable phase is formed within the bulk metastable phase, in the absence of a preexisting interface [4]. Since homogeneous nucleation in superheated liquids involves forming sufficiently large voids, it is natural to inquire whether voids in inherent structures are related to regions of low density, or "weak spots" in the unquenched superheated liquid that could act as nucleating sites for boiling or cavitation.

To answer this question, we examine the void space geometry of configurations of the shifted-force Lennard-Jones fluid. As explained in Fig. 1, each vertex of the Voronoi polyhedron associated with any given atom is the center of a Delaunay tetrahedron. This Voronoi vertex is the center of a Delaunay circumsphere. The difference between the circumsphere's diameter and the Lennard-Jones size parameter σ defines the size of the void associated with the Voronoi vertex. The maximum void size associated with an atom's Voronoi polyhedron defines the single void size assigned to an atom in any configuration under study [16]. This constitutes a measure of local density fluctuations towards lower-density values, which are important in superheated liquids. Having thus assigned a void size to each atom, we ask whether a given atom, upon steepest-descent quenching onto a mechanically stable inherent structure, becomes a bulk or a surface atom, as defined in Sec. IV. This is repeated several times, to gather statistics. Finally, we calculate, at a given temperature and density, the probability that atoms associ-
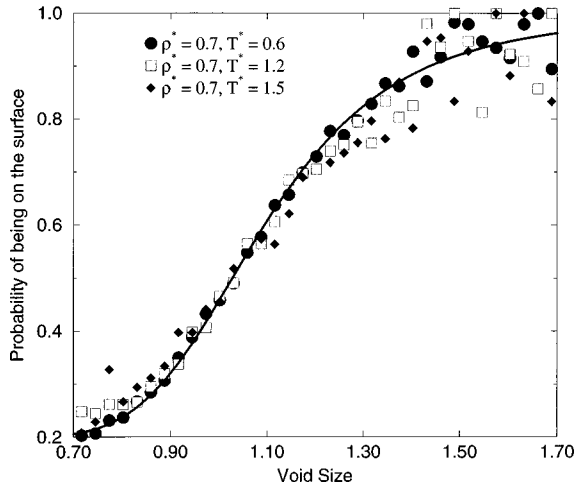
FIG. 9. Correlation between the void size assigned to an atom in the equilibrium configuration (in units of σ) and the probability that the atom is a surface atom in the inherent structure, at several temperatures, for $\rho^* = 0.7$. The continuous line is drawn as a smooth fit to the data at $\rho^* = 0.7$, $T^* = 0.6$.

ated with a given void size end up as surface atoms (i.e., atoms associated with the largest cavity in the inherent structure). This amounts to asking whether the appearance of large voids (weak spots) in the liquid is associated with the appearance of inhomogeneous inherent structures. The result is shown in Fig. 9. The three curves correspond to calculations performed at a single density ($\rho^* = 0.7$, which is close to the triple point), and at temperatures spanning a range from subtriple to supercritical.

At each of the three temperatures investigated, there is a void size $d_{min} \sim 0.5\sigma$ [16] such that atoms associated with voids larger than d_{min} are increasingly likely to end on the inherent structure interface, this probability increasing with void size. The steepness of the interface probability vs void size curve decreases with increasing temperature.

These calculations show that small voids ($d < d_{min}$) form spontaneously and frequently, as a result of thermally driven density fluctuations. The formation of large ($d > d_{min}$) voids, on the other hand, requires favorable energetics, and this is reflected in the geometry of underlying inherent structures. Temperature, therefore, affects the formation of cavities in two ways: it is solely responsible for the formation of small voids that result from density fluctuations, and it affects the rate at which the energy landscape is traversed. This traversal provides the favorable energetics needed for forming large voids, or weak spots. Questions worth examining include the temperature- and density-dependent rate of formation of weak spots of a given size, the energetics of weak spot formation, and the fate of weak spots after they are formed. Clearly, answers to these questions should provide a firm basis on which an improved, molecular-based understanding of cavitation and homogeneous nucleation in superheated liquids can be built.

The preceding discussion addressed some possible implications of inhomogeneous inherent structures for cavitation and nucleation. We now turn our attention to the inherent structures themselves, and to the thermodynamic implications of their inhomogeneity. Figure 8 shows the equation of state of the inherent structures over the density range ρ^*

$= 0.6$ (2.4 times the critical density) to 1.05 (1.57 times the liquid's triple point density). It is natural to inquire whether the mechanical instability at $\rho^* = 0.89$ bears any relationship to the $T = 0$ limit of the superheated liquid spinodal. To this end, we calculate the ratio of the maximum tensile strength to the critical pressure. For the van der Waals fluid this quantity equals 27; for the shifted-force Lennard-Jones fluid, the ratio is 30. This close agreement suggests that the equation of state of the inherent structures may be thought of as the $T = 0$ limit of the fluid's equation of state. According to this interpretation, the inhomogeneous nature of inherent structures would correspond to spinodally decomposed structures, arrested at $T = 0$. Furthermore, the $T = 0$ limit of the superheated liquid spinodal would define a limiting density, above which inherent structures are homogeneous and below which they are fissured, with possible consequences for the glass transition, insofar as glasses may only be formed at densities higher than this spinodal density. Of course, the validity of this ''fluidlike'' interpretation of structures whose constituent particles by definition lack any mobility whatsoever, needs to be critically examined.

VI. DISCUSSION

In this work we have determined and interpreted the statistical geometry of fluctuating void space in a model atomic liquid. Calculations have been done both for liquid configurations and for their mechanically stable inherent structures generated by steepest-descent quenching onto local potential energy minima. Both stable and metastable states have been considered. The most important findings are as follows.

(1) There exists a well-defined bulk density above which inherent structures are homogeneous, and below which they are fissured due to the appearance of large voids.

(2) Large voids appear in the inherent structures as a result of mechanical instability such that on further decrease of the bulk density, tension is relieved and the pressure increases towards positive values.

(3) This mechanical instability appears to be the $T = 0$ extrapolation of the superheated liquid spinodal.

(4) Insofar as a glass can be considered a liquid trapped in an inherent structure, the mechanical instability may be an absolute lower density limit to the possibility of glass formation.

(5) Weak spots, that is to say large voids that serve to initiate bubble nucleation, form as a result of sampling local potential minima that provide the requisite favorable energetics.

(6) The quantitative investigation of the density- and temperature-dependent kinetics of weak spot formation should provide a microscopic basis for the formulation of a rigorous theory of bubble nucleation of liquids.

Our analysis has been restricted to a simple model atomic liquid. We are pursuing the extension of this approach to molecular liquids, and in particular, water. Here, the statistical geometry of fluctuating void space, especially under conditions of negative expansivity, that is to say when the temperature and pressure, or energy and volume, are anticorrelated, should prove useful in understanding the still intriguing properties of water at low temperatures [4]. Finally, the determination and interpretation of weak spot for-

mation may also prove useful for understanding mechanical failure of materials at interfaces. Questions worth examining here include the role of surface inhomogeneity in creating favorable energetics for weak spot formation, and the fate of these weak spots once formed.

ACKNOWLEDGMENTS

APPENDIX A: VIRIAL EXPRESSION FOR PRESSURE IN SIMULATIONS WITH PERIODIC BOUNDARY CONDITIONS

The pressure is routinely calculated in simulations using the virial function. However, in simulations where periodic boundary conditions are employed, the separation of forces on particles into internal and external or ''wall'' forces is not straightforward and hence the relation of the virial calculated in simulations with thermodynamic pressure is subtle. Further ambiguities arise in calculating pressure in this manner for the inherent structures, in which each particle experiences zero net force, since an inherent structure is defined to be a mechanically stable configuration of particles. Hence we discuss below details leading to the identification of the virial expression as calculated in simulations with the pressure experienced by the simulated system. A discussion of this issue for hard core systems may be found in [17].

Consider initial ($t=0$) particle positions $\mathbf{r}_1, \mathbf{r}_2, \ldots$ in the primary cell

$$0 \leq x < L_x,$$

$$0 \leq y < L_y,$$

$$0 \leq z < L_z. \tag{A1}$$

The cell volume is given by

$$V = L_x L_y L_z. \tag{A2}$$

The Newtonian equations of motion

$$m_i \frac{d^2 \mathbf{r}_i}{dt} = \mathbf{F}_i \quad (i = 1, 2, \ldots, N) \tag{A3}$$

determine $\mathbf{r}_i(t)$ for $t > 0$, where m_i is the mass of particle i, and $\mathbf{F}_i$ is the force it experiences from all other particles and their images in the periodic replicas of the primary cell. The Newtonian dynamics can cause $\mathbf{r}_i(t)$ to leave the primary cell, and as it does so, an image particle simultaneously enters at the opposite face. Let $\mathbf{r}_i^*(t)$ be the position of i or that one of its images which is in the primary cell at time t. We can write

$$\mathbf{r}_i(t) = \mathbf{r}_i^*(t) + n_x(t) L_x \mathbf{u}_x + n_y(t) L_y \mathbf{u}_y + n_z(t) L_z \mathbf{u}_z$$

$$\equiv \mathbf{r}_i^*(t) + \boldsymbol{\Delta}_i(t), \tag{A4}$$

where $\mathbf{u}_x$, $\mathbf{u}_y$, and $\mathbf{u}_z$ are unit vectors along each of the three Cartesian axes, and n_x, n_y, and n_z are signed integers that track crossings of cell boundaries.

Following Clausius, the conventional virial is defined as

$$\mathcal{V} = \sum_i^N \mathbf{r}_i \cdot \mathbf{F}_i. \tag{A5}$$

On account of the periodic boundary conditions, we also need to consider the variant

$$\mathcal{V}^* = \sum_i^N \mathbf{r}_i^* \cdot \mathbf{F}_i. \tag{A6}$$

We first carry out the usual analysis for $\mathcal{V}$, which can be rewritten, using Eq. (A3), as

$$\mathcal{V} = \sum_{i=1}^N m_i \mathbf{r}_i \cdot \frac{d^2 \mathbf{r}_i}{dt^2}. \tag{A7}$$

Calculate the time average $\bar{\mathcal{V}}$ over $0 \leq t \leq t_0$, where t_0 will eventually be allowed to become infinite.

$$\bar{\mathcal{V}} = \frac{1}{t_0} \int_0^{t_0} \mathcal{V} dt = \frac{1}{t_0} \int_0^{t_0} \sum_i m_i \left(\mathbf{r}_i \cdot \frac{d^2 \mathbf{r}_i}{dt^2} \right) dt$$

$$= -\frac{1}{t_0} \int_0^{t_0} \sum_i m_i \left(\frac{d\mathbf{r}_i}{dt} \right)^2 dt + \frac{1}{t_0} \left[\sum_i m_i \mathbf{r}_i \cdot \frac{d\mathbf{r}_i}{dt} \right]_0^{t_0}$$

$$= -2\bar{K} + \frac{1}{2t_0} \left[\sum_i m_i \frac{d}{dt} (r_i^2) \right]_0^{t_0}, \tag{A8}$$

where K represents the system's total kinetic energy. Assuming that the system approaches an equilibrium state in the long time limit, we can relate $\bar{K}$ to the kinetic temperature T,

$$\lim_{t_0 \to \infty} \bar{K} = \tfrac{3}{2} N k_B T. \tag{A9}$$

Note also that

$$\frac{d}{dt} (r_i^2) \bigg|_{t=0} = \text{finite},$$

$$\frac{d}{dt} (r_i^2) \bigg|_{t_0} \sim 6 D_i, \tag{A10}$$

where D_i is the diffusion constant of species i, also a finite quantity. Consequently the last term in Eq. (A8) vanishes in the $t_0 \to \infty$ limit, and we have in that limit

$$\bar{\mathcal{V}} = -2\bar{K} = -3 N k_B T. \tag{A11}$$

The second of Eqs. (A10) assumes that there is no center of mass drift for the coordinates $\mathbf{r}_i$.

Because the $\mathbf{r}_i(t)$ diffuse without bound throughout the infinite periodic array of cells, there is no obvious way at

long times to resolve the $\mathbf{F}_i$ into ''wall'' and ''internal'' components. However, this can be done in the case of $\mathcal{V}^*$, as we explain below. First, we invoke Eqs. (A4)–(A6), and write

$$\bar{\mathcal{V}}^* = \bar{\mathcal{V}} - \frac{1}{t_0} \int_0^{t_0} \sum_i \boldsymbol{\Delta}_i(t) \cdot \mathbf{F}_i(t) dt. \qquad (A12)$$

From its definition in Eq. (A4), $\boldsymbol{\Delta}_i(t)$ is a piecewise constant vector, which tracks the diffusive process for particle i in a coarse-grained way, identifying only the cell of residence at any given t. But because this is so, $|\boldsymbol{\Delta}_i|$ will tend to increase as $t^{1/2}$ at long times. Except possibly at short times, $\boldsymbol{\Delta}_i$ and $\mathbf{F}_i$ should be uncorrelated (i.e., the position of a particle is uncorrelated with the force acting on it), so

$$\lim_{t_0 \to +\infty} \frac{1}{t_0} \int_0^{t_0} \boldsymbol{\Delta}_i(t) \cdot \mathbf{F}_i(t) dt = 0. \qquad (A13)$$

Therefore, in the $t_0 \to +\infty$ limit,

$$\bar{\mathcal{V}}^* = \bar{\mathcal{V}} = -3Nk_BT, \qquad (A14)$$

and so $\bar{\mathcal{V}}^*$ can be used to derive the usual virial equation of state.

Consider the usual separation into external and internal forces as is written in the derivation of the virial-explicit equation of state [18]:

$$\bar{\mathcal{V}} = -3Nk_BT = \left\langle \sum_i \mathbf{r}_i \cdot \mathbf{F}_i^{\text{ext}} \right\rangle + \left\langle \sum_i \mathbf{r}_i \cdot \mathbf{F}_i^{\text{int}} \right\rangle. \quad (A15)$$

The external part of the above expression is calculated by writing $\langle \Sigma_i \mathbf{r}_i \cdot \mathbf{F}_i^{\text{ext}} \rangle = -\oint (\mathbf{r} \cdot \mathbf{n}) P dA = -P \int (\boldsymbol{\nabla} \cdot \mathbf{r}) dV = -3PV$, where $\mathbf{n}$ is the local unit normal vector pointing away from the center of the cell, and $\mathbf{r}$ is the position vector on the wall [18]. Hence

$$\bar{\mathcal{V}} = -3Nk_BT = -3PV + \left\langle \sum_i \mathbf{r}_i \cdot \mathbf{F}_i^{\text{int}} \right\rangle, \qquad (A16)$$

which leads to the familiar expression for pressure,

$$PV = Nk_BT + \frac{1}{3} \left\langle \sum_i \mathbf{r}_i \cdot \mathbf{F}_i^{\text{int}} \right\rangle \equiv Nk_BT + \frac{1}{3} \langle \mathcal{V}^{\text{int}} \rangle. \qquad (A17)$$

We now describe the separation of the total force into internal and external forces in a simulation, and the identification of the external forces with the pressure term in the virial expression. In this discussion, we specialize to short-ranged, pairwise central potentials, such that for any given pair of atoms i and j, there is only one force term acting on i arising from j and all its periodic images. Further, we consider a cubic simulation box of dimension L. With pairwise interactions, we may write $\mathbf{F}_i = \Sigma_{j \neq i} \mathbf{F}_{ij}$, with $\mathbf{F}_{ij} = -\mathbf{F}_{ji}$. We can thus write

$$\langle \mathcal{V}^{\text{int}} \rangle = \sum_i \left\langle \mathbf{r}_i \cdot \left(\sum_{j \neq i} \mathbf{F}_{ij} \right) \right\rangle. \qquad (A18)$$

This can be rearranged to obtain, with $r_{ij} = |\mathbf{r}_i - \mathbf{r}_j|$, and ϕ_{ij} the pair potential,

$$\langle \mathcal{V}^{\text{int}} \rangle = -\sum_{i,j>i} \left\langle r_{ij} \frac{\partial \phi_{ij}}{\partial r_{ij}} \right\rangle. \qquad (A19)$$

Now consider the simulated system with periodic boundary conditions, where the force on a particle in the primary cell can be written as $\mathbf{F}_i = \Sigma_{j \neq i, \mathbf{w}} \mathbf{F}_{ij\mathbf{w}}$, where the vector $\mathbf{w}$ labels the periodic images of j, and is of the form $(n_x, n_y, n_z) \equiv n_x \mathbf{u}_x + n_y \mathbf{u}_y + n_z \mathbf{u}_z$. The periodic image has coordinates displayed by $L(n_x \mathbf{u}_x + n_y \mathbf{u}_y + n_z \mathbf{u}_z) = L\mathbf{w}$. Thus $\Sigma_{\mathbf{w}}$ stands for three embedded summations of the integer indices n_x, n_y, and n_z. For short-range forces (range $< L/2$) only one image of particle j (including the primary cell) contributes a finite force. Let $\mathbf{w}_j$ index such a periodic image. The total virial is then written as

$$\langle \mathcal{V}^* \rangle = \sum_i \sum_{j \neq i, \mathbf{w}} \langle \mathbf{r}_i^* \cdot \mathbf{F}_{ij\mathbf{w}} \rangle = \frac{1}{2} \sum_i \sum_{j \neq i, \mathbf{w}} \langle (\mathbf{r}_i^* - \mathbf{r}_j^*) \cdot \mathbf{F}_{ij\mathbf{w}} \rangle$$

$$= \frac{1}{2} \sum_i \sum_{j \neq i} \langle (\mathbf{r}_i^* - \mathbf{r}_j^*) \cdot \mathbf{F}_{ij\mathbf{w}_j} \rangle. \qquad (A20)$$

Note that $(\mathbf{r}_i^* - \mathbf{r}_j^*)$ is not the vector displacement from atom i to the particular image of j which exerts a finite force on i, and consequently $(\mathbf{r}_i^* - \mathbf{r}_j^*)$ is not parallel to $\mathbf{F}_{ij\mathbf{w}_j}$. We rewrite this expression by adding and subtracting the vector $\mathbf{w}_j L$. Thus

$$\langle \mathcal{V}^* \rangle = \frac{1}{2} \sum_i \sum_{j \neq i} \langle (\mathbf{r}_i^* - \mathbf{r}_j^* - \mathbf{w}_j L) \cdot \mathbf{F}_{ij\mathbf{w}_j} \rangle$$

$$+ \frac{L}{2} \sum_i \sum_{j \neq i} \langle \mathbf{w}_j \cdot \mathbf{F}_{ij\mathbf{w}_j} \rangle \equiv \langle \mathcal{V}^{\text{sim}} \rangle + \langle \mathcal{V}^{\text{ex}} \rangle. \qquad (A21)$$

The first term $\langle \mathcal{V}^{\text{sim}} \rangle$ is what one calculates in simulations to be the virial [19]. The second term contains a sum over all forces that are due to image particles, which lie outside the primary cell, multiplied vectorially with displacements from the particle coordinates in the primary cell to the image locations. Along each Cartesian direction ($\pm x, \pm y, \pm z$), if the appropriate sum of normal component of forces is equated with the pressure times the surface area, with the total virial being equal to $3Nk_BT$, the result of the above expression is

$$PV = Nk_BT + \frac{1}{3} \langle \mathcal{V}^{\text{sim}} \rangle. \qquad (A22)$$

Thus the pressure of an inherent structure is in general nonzero, even though the net force on every atom is zero, and $T = 0$.

APPENDIX B: MORPHOLOGY OF INHERENT STRUCTURES

Figure 8 identifies the density $\rho^*=0.89$ as the point of maximum tension for liquid-phase inherent structures. Our analysis indicates further that when $\rho^*<0.89$, large voids appear in the inherent structures. The numerical simulations have been restricted to modest numbers of particles for obvious practical reasons, but it seems reasonable to suppose that much larger, even macroscopic systems in the same low-density range would also exhibit a corresponding fraction of large-void empty space in their inherent structures. Still left unanswered is a basic question about the geometric character of this inherent structure empty space in the large-system limit. One possibility is that during the steepest-descent quenching most of the large voids aggregate to produce a macroscopic, more or less compact, empty region, loosely speaking a ''vacuum phase.'' A second possibility is that the voids, perhaps relatively large compared to particle diameter σ, remain dispersed throughout the medium.

This appendix provides a simple heuristic argument that favors the second alternative over the first. Subsequent simulations with substantially larger systems may be able to confirm or reject that conclusion. But if it turns out to be incorrect, the reason for its failure will have to involve some deep and unsuspected characteristic of the steepest-descent mapping that generates liquid-phase inherent structures.

In the low-density regime under consideration, attractive interparticle interactions are a decisive feature for the attainment of inhomogeneous structures as a result of applying the steepest-descent operation defined by Eq. (11). In the early stage of that operation, small groups of particles draw together in a coarsening process that simultaneously must begin to leave behind low-density spots of comparable size. The coarsening process continues as the small aggregates are attracted to one another and combine (with suitable readjustments) to form larger dense aggregates.

Let $l(s)$ be a coherence or correlation length for spatial density fluctuations in the partially quenched medium. It can equally well be described as the mean aggregate size at virtual time s in the steepest-descent mapping, Eq. (11). The mean spatial extent of void regions created by the coarsening process hence should also be proportional to some multiple of this length, say $\theta(\rho^*)l(s)$. We wish to determine whether

$$\lim_{s\to\infty} l(s) \tag{B1}$$

exists and is equal to some well-defined limit $l_\infty(\rho^*)$ even for arbitrarily large systems, or whether the expression Eq. (B1) diverges to infinity for arbitrarily large systems. In either case, it is reasonable to assume that $l(s)$ increases monotonically with s. Especially during the late stages of steepest-descent quenching, configurational readjustments have a distinctive intermittent, or sporadic, character. This is vividly evident when virtual time s is eliminated and the potential energy Φ is plotted against $|\nabla\Phi|$ or $|\nabla\Phi|^2$ for the quench [20,21]. These episodes have a natural interpretation as sudden relative motions of essentially solid particle domains to produce larger groupings, and this is exactly the coarsening process described above and monitored by the coherence length $l(s)$. A facile analogy for the intermittency, from geology, is the sudden realignment of tectonic plates marked by earthquakes.

The key question to be answered is whether at stage $l(s)$ attractive forces are sufficiently powerful to drive the system towards further consolidation. Consider the net attractive force acting between a pair of compact domains of linear dimension comparable to $l(s)$ and separated by a void or fissure also of width comparable to $l(s)$. The magnitude of this net force can be expressed as the following integral over the volumes V_1 and V_2 occupied by these domains:

$$F=\rho_a^2\int_{V_1}d\mathbf{r}_i\int_{V_2}d\mathbf{r}_j|\nabla v(r_{ij})\cdot\mathbf{u}_{12}|. \tag{B2}$$

In this expression, ρ_a stands for the particle density inside each of the (amorphous) domains, $v(r_{ij})$ is the particle pair potential that supplies the attraction, and $\mathbf{u}_{12}$ is a unit vector along the line of centers between the domains. Realistic molecular interactions between uncharged and nonpolar species are dominated by dispersion interactions at long range; in the conventional Lennard-Jones terminology we can set

$$v(r_{ij})\simeq-4\epsilon(\sigma/r_{ij})^6. \tag{B3}$$

Consequently Eq. (B2) becomes

$$F=-24\rho_a^2\epsilon\sigma^6\int_{V_1}d\mathbf{r}_i\int_{V_2}d\mathbf{r}_j r_{ij}^{-7}\cos(\mathbf{u}_{ij}\cdot\mathbf{u}_{12}), \tag{B4}$$

where $\mathbf{u}_{ij}=\mathbf{r}_{ij}/r_{ij}$. Assuming that the shape and orientations of V_1 and V_2 remain fixed, and that their separation maintains a constant ratio with their size, it is easy to see that F scales inversely with the coherence length $l(s)$.

$$F\propto 1/l(s), \tag{B5}$$

so the net attraction diminishes to zero with increasing $l(s)$. Of course our simulations described earlier have used the finite cutoff version of the Lennard-Jones potential and so have an even weaker effect at large $l(s)$ than that shown in Eq. (B5), namely, vanishing identically when the gap between domains exceeds the cutoff distance.

In order for F to succeed in pulling together domains V_1 and V_2 (and consequently combining void spaces in the neighborhood) it must overcome the restoring forces F' that attach them to other neighboring domains. It can be argued that F' should scale as a positive power of $l(s)$:

$$F'=[l(s)]^p, \quad p>0. \tag{B6}$$

The area of attachment along a relatively poorly bonded boundary between contacting domains should, on average, be proportional to $[l(s)]^2$, i.e., $p=2$. Alternatively, if elastic deformation of the local domain complex is required to bridge the gap between V_1 and V_2, then $p=3$. So long as p is positive as indicated in Eq. (B6), its precise value need not be known.

The nature of the steepest-descent process at large $l(s)$ depends on which of F and F' dominates. In the earliest

stages it is clearly the attractive forces, i.e., F, that drive the mapping to minima. However, it is obvious from comparison of characteristic dependences on $l(s)$ in Eqs. (B5) and (B6) that a crossover at finite l must occur. At this point, further coarsening becomes infeasible. The consolidation process halts at finite coherence length $l_\infty(\rho^*)$.

This argument leaves unspecified the geometric nature of the void space at the termination of the arrested consolidation process. It may consist of relatively large but disconnected voids. Or it may be above the void space percolation threshold to produce a bicontinuous texture of interpenetrating and multiply connected regions of dense amorphous matter and of empty space.

---

[1] P. A. Egelstaff, *An Introduction to the Liquid State*, 2nd ed. (Clarendon, Oxford, 1992), Chap. 3.

[2] J.-P. Hansen and I. R. McDonald, *Theory of Simple Liquids*, 2nd ed. (Academic, London, 1986).

[3] D. S. Corti, P. G. Debenedetti, S. Sastry, and F. H. Stillinger, Phys. Rev. E **55**, 5522 (1997).

[4] P. G. Debenedetti, *Metastable Liquids* (Princeton University Press, Princeton, NJ, 1996).

[5] W. Alter, J. Chem. Phys. **5**, 577 (1937).

[6] R. Fürth, Proc. Cambridge Philos. Soc. **37**, 252 (1941).

[7] J. Frenkel, *Kinetic Theory of Liquids* (Dover, New York, 1955), p. 174.

[8] J. O. Hirschfelder, C. F. Curtiss, and R. B. Bird, *Molecular Theory of Gases and Liquids* (Wiley, New York, 1954), p. 1041.

[9] F. H. Stillinger and T. A. Weber, J. Chem. Phys. **83**, 4767 (1985).

[10] W. H. Press, S. A. Teukolsky, W. T. Vetterling, and B. P. Flannery, *Numerical Recipes*, 2nd ed. (Cambridge University Press, Cambridge, England, 1992).

[11] M. Tanemura, T. Ogawa, and N. Ogita, J. Comput. Phys. **51**, 191 (1983).

[12] S. Sastry, D. S. Corti, P. G. Debenedetti, and F. H. Stillinger, preceding paper, Phys. Rev. E **56**, 5524 (1997).

[13] J. L. Finney and J. Wallace, J. Non-Cryst. Solids **43**, 165 (1981).

[14] F. H. Stillinger, Science **267**, 1935 (1995).

[15] R. A. LaViolette, Phys. Rev. B **40**, 9952 (1989).

[16] The distribution of such maximum void sizes assigned to each atom is clearly different from the overall void size distribution. The probability of occurrence of maximum void size below $d_{min} \sim 0.5\sigma$ and greater than $d_{max} \sim 2.0\sigma$ is found to be negligible for $\rho^* = 0.7$. The value of d_{min} corresponds roughly to the void size where the overall probability distribution is maximum, while d_{max} corresponds to the largest void sizes with finite probability in the overall void size distribution.

[17] J. J. Erpenbeck and W. W. Wood, in *Statistical Mechanics B. Modern Theoretical Chemistry*, edited by B. J. Berne (Plenum, New York, 1981), Vol. 6, pp. 1–40.

[18] L. D. Landau and E. M. Lifshitz, *Statistical Physics Part 1*, 3rd ed. (Pergamon, Oxford, 1980), p. 94.

[19] M. P. Allen and D. J. Tildesley, *Computer Simulation of Liquids* (Clarendon, Oxford, 1992).

[20] F. H. Stillinger and T. A. Weber, Phys. Rev. A **25**, 978 (1982) (see Fig. 2).

[21] D. S. Corti, Ph.D. thesis, Princeton, 1996 (see Fig. 5.2).